Clim Dyn (2016) 46:619–636
DOI 10.1007/s00382-015-2602-5

Inhomogeneous warming of the Tropical Indian Ocean in the CMIP5 model simulations during 1900–2005 and associated mechanisms

Shuai-Lei Yao[1,2] · Gang Huang[1,3] · Ren-Guang Wu[4,1] · Xia Qu[4] · Dong Chen[4,2]

Received: 14 August 2014 / Accepted: 8 April 2015 / Published online: 3 May 2015

Abstract The characteristics and causes of inhomogeneous warming of the Tropical Indian Ocean (TIO) sea surface temperature during 1900–2005 are investigated based on observations and 16 Coupled Model Intercomparison Project phase 5 (CMIP5) models. Over the TIO, the observed warming trend has more than doubled since 1965, which is well simulated by the CMIP5 historical runs. However, as to spatial warming pattern, observations manifest a double-peak pattern during 1900–1940 and a non-uniform Indian Ocean Mode (IOBM)-like pattern during 1965–2005, which is not captured by the CMIP5 historical runs. Herein, an optimal detection analysis is employed, which indicates that the double-peak warming pattern can be explained well by a combination of Greenhouse Gas (GHG) and natural forcing, and the non-uniform IOBM-like pattern is mostly attributable to anthropogenic forcing. Further, a mixed-layer heat budget analysis shows that atmospheric and oceanic processes, especially latent heat flux from atmospheric forcing part associated with GHG forcing, are beneficial for the warming patterns formation. Our study supports the claim that intrinsic ocean–atmosphere interaction within the TIO is the key mechanism for maintaining the TIO warming. From the model perspective, during 1900–1940, the weak anti-symmetric atmospheric circulation with easterly (northwesterly) anomalies north (south) of the equator helps to sustain the double-peak warming pattern. During 1965–2005, the intensified anti-symmetric wind pattern is in favor of the non-uniform IOBM-like warming pattern.

Keywords Tropical Indian Ocean · Inhomogeneous warming · Double-peak warming pattern · Non-uniform IOBM-like pattern · Anti-symmetric atmospheric circulation

1 Introduction

About 84 % of the total heating of the Earth system has been absorbed by ocean (Levitus et al. 2005). Due to its thermal inertia, ocean retards the pace of the global warming by absorbing a majority of solar heating trapped by well-mixed Greenhouse Gas (GHG) forcing (Hegerl and Bindoff 2005). The signature of widespread warming in sea surface temperature (SST) emerges most clearly when considering the global ocean for much of the twentieth century based on a wide range of observations (Stocker et al. 2013). Much attention has been directed to each ocean basin for time spans of a decade or more. The Indian Ocean exhibits a robust basin-wide SST warming since the 1950s (Du and Xie 2008; Hoerling et al. 2004), amounting to the order of 0.5 °C over the past 50 years, though the strong warming signal is not monotonic (Levitus et al. 2000).

Observations and numerical experiments have shown some distinctive spatial features in the Indian Ocean warming signal. Levitus et al. (2005) stressed that the Indian Ocean heat storage has displayed a pronounced increase

✉ Gang Huang
hg@mail.iap.ac.cn

[1] State Key Laboratory of Numerical Modeling for Atmospheric Sciences and Geophysical Fluid Dynamics, Institute of Atmospheric Physics, Chinese Academy of Sciences, P. O. Box 9804, Beijing 100029, China

[2] University of Chinese Academy of Sciences, Beijing 100049, China

[3] Joint Center for Global Change Studies, Beijing 100875, China

[4] Center for Monsoon System Research, Institute of Atmospheric Physics, Chinese Academy of Sciences, Beijing 100029, China

in the upper 700 m in the southern Indian Ocean, but kept roughly constant for the northern Indian Ocean over the past 5 decades, which is partly associated with a hemispheric difference in the net surface heat flux caused by the buildup of aerosols over the northern Indian Ocean. Furthermore, by analyzing a new Indian Ocean Temperature Archive (IOTA), Alory et al. (2007) reported a particularly significant warming signal in the western subtropical Indian Ocean from 40 to 50°S extending to 800 m; in contrast, a remarkable warming from 15°S to 5°N was confined to above the 20 °C isotherm, along with a pronounced subsurface cooling in the depth of 100–200 m. Harrison and Carson (2007) pointed out that it was difficult to make an accurate determination of heat storage trend because of the sparse data coverage in the Indian Ocean, especially the southern Indian Ocean. It is indicated that the Tropical Indian Ocean (TIO) warming is mainly trapped in the top 125 m (Pierce et al. 2006). Climate models exhibit an appreciable warming of IOD-type pattern with warming in the western TIO and cooling in the southeastern TIO (Vecchi and Soden 2007; Zheng et al. 2010). The confidence level of the temporal and spatial characteristics in the TIO warming signal is low due to the lack of a multi-model ensemble mean approach.

The Indian Ocean warming has remote impacts on regional climate change. A large body of model simulations have demonstrated that the warming in the Indian Ocean is at least partly responsible for droughts over the Sahel and other parts of Africa (Bader and Latif 2003; Giannini et al. 2003; Hoerling et al. 2006), the prolonged droughts during 1998–2002 over North America, the Mediterranean, and the Middle East (Hoerling and Kumar 2003), and trends in the North Atlantic Oscillation and annular modes (Hoerling et al. 2004; Lu et al. 2004). Additionally, the warming trend influences Australian precipitation (Ashok et al. 2003), Indian monsoon circulation (Krishnan et al. 2006) and East Asian monsoon circulation (Li et al. 2010) as well as the extra-tropical remote forcing of ENSO (Lau et al. 2006). Numerical model simulations are capable of supporting observational evidence that the TIO warming is a key forcing for the northwestern Pacific and East Asian climate change in the 1970s (Xie et al. 2010b). Therefore, understanding the causes of the TIO warming is an essential scientific basis for future regional climate projection with improved skill and reduced uncertainty.

A wide variety of relevant mechanisms have been proposed for the Indian Ocean warming. For one thing, many coupled ocean–atmosphere models have reproduced the warming in the TIO when forced by external forcing, especially by increased GHG and aerosol concentrations (Alory et al. 2007; Barnett et al. 2005; Hoerling et al. 2004; Pierce et al. 2006), but the warming signal has not been found when anthropogenic forcing is absent (Knutson et al. 2006). Barnett et al. (2005) stated that the increased heat content of the northern Indian Ocean was mainly induced by the ocean temperature advection, whereas other parts of the Indian Ocean were subjected to increasing surface heat fluxes. Du and Xie (2008) further suggested that GHG forcing may have contributed significantly to the warming in the TIO. Moreover, the thermocline change induced by ocean waves (Li et al. 2003) and a deceleration of the wind-driven Ekman pumping (Alory and Meyers 2009) are also regarded as the dominant causes. For another, internally-generated variability of the climate system is a possible explanation. The 1976–1977 climate regime shift over the Pacific Ocean has promoted the basin-wide warming over the Indian Ocean (Terray and Dominiak 2005). Despite so many mechanisms posed, the pivotal physical mechanism responsible for the TIO warming, however, is still unclear.

The purpose of the present study is to identify the major spatio-temporal features of changes in the TIO SST and to investigate relevant mechanisms. Our study extends 10 IPCC-AR4 models assessment (Alory et al. 2007). We not only evaluate the latest 16 CMIP5 models, but more importantly, shed light on the key role of intrinsic ocean–atmosphere interaction and ocean dynamics within the TIO in sustaining the inhomogeneous warming signal. We mainly put a spotlight on spatio-temporal pattern of the TIO warming and concerned formation mechanisms. Our study may therefore provide a possible explanation of physical processes at work in the real ocean and responsible for the observed inhomogeneous warming in the TIO.

The rest of the paper is arranged as follows. Details on the observations, model simulations and diagnostic methods are described in Sect. 2. Major features and causes of the TIO warming based on observations and multi-model ensemble means are given in Sect. 3. The main conclusions and discussions on the findings from this study are presented in Sect. 4.

2 Model, observations and analysis methods

2.1 Model and experiments

This study adopts the total 180 simulations from the World Climate Research Program's Coupled Model Intercomparison Project phase 5 (CMIP5) models organized by the U.S. Department of Energy's Program for Climate Model Diagnosis and Intercomparison (PCMDI) in support of the Intergovernmental Panel on Climate Change Fifth Assessment Report (IPCC-AR5), which include 71 historical, 45 historicalGHG, 48 historicalNat and 16 piControl realizations (Table 1), respectively. Here we mainly analyze six sets of simulations (Taylor et al. 2012). The historical simulations (named as ALL) are forced by both anthropogenic

Table 1 Technical details of 16 CMIP5 Models used in this study

No.	Model	Institute	Atmospheric resolution (lat × lon)	N_H	N_G	N_N	N_C
1	bcc-csm1-1	BCC/China	64 × 128	3	1	1	1
2	BNU-ESM	GCESS/China	64 × 128	1	1	1	1
3	CCSM4	NCAR/USA	192 × 288	6	3	4	1
4	CanESM2	CCCMA/Canada	64 × 128	5	5	5	1
5	CNRM-CM5	CNRM-CERFACS/France	128 × 256	10	6	6	1
6	CSIRO-Mk3-6-0	CSIRO-QCCCE/Australia	96 × 192	10	5	5	1
7	GFDL-CM3	NOAA GFDL/USA	90 × 144	5	3	3	1
8	GFDL-ESM2 M	NOAA GFDL/USA	90 × 144	1	1	1	1
9	GISS-E2-H	NASA GISS/USA	90 × 144	5	5	5	1
10	GISS-E2-R	NASA GISS/USA	90 × 144	6	5	5	1
11	IPSL-CM5A-LR	IPSL/France	96 × 96	6	3	3	1
12	IPSL-CM5A-MR	IPSL/France	143 × 144	3	3	3	1
13	MIROC-ESM	MIROC/Japan	64 × 128	3	1	3	1
14	MIROC-ESM-CHEM	MIROC/Japan	64 × 128	1	1	1	1
15	MRI-CGCM3	MRI/Japan	160 × 320	3	1	1	1
16	NorESM1-M	NCC/Norway	96 × 144	3	1	1	1
	Total	–	–	71	45	48	16

Official model acronyms, their institutes, Atmospheric General Circulation Model (AGCM) horizontal grid resolution, and the number of realizations from historical runs (N_H), historicalGHG runs (N_G), historicalNat runs (N_N), and preindustrial control integrations (N_C) are listed, respectively

forcing (well-mixed GHGs and human-induced aerosols) and natural forcing (solar irradiance changes and volcanic aerosols). The historicalGHG (named as GHG) and historicalNat (named as NAT) simulations are consistent with the ALL except that they are forced by well-mixed greenhouse gases and natural forcing only, respectively. The piControl (named as INT) experiment is a long-term simulation with imposed non-evolving, pre-industrial conditions, including prescribed atmospheric concentrations (all well-mixed gases and some short-lived species), non-evolving emissions or concentrations (natural aerosols or their precursors, some reactive species), and even unperturbed land use. Besides, according to Taylor et al. (2009), the difference between historical and historicalNat runs is defined as anthropogenic simulations (named as ANT). Likewise, the difference between anthropogenic and historicalGHG runs is characterized as aerosol simulations (named as AER). In this study, we apply outputs from a total of 16 different CMIP5 models, including SST, surface heat flux (shortwave and longwave radiation, latent heat flux and sensible heat flux), surface wind, near-surface wind speed, precipitation and sea surface height.

2.2 Observational datasets

The observations used here include: (1) the monthly mean SST from the Hadley Centre Global Sea Ice and Sea Surface Temperature (HadISST) analysis data for the period 1900–2005 (Rayner et al. 2003), with a spatial resolution of 1° latitude × 1° longitude; (2) version 3b of the National Oceanic and Atmospheric Administration Extended Reconstructed Sea Surface Temperature (ERSST_V3b) data for the period 1900–2005 in the form of monthly mean on a regular 2° × 2° latitude/longitude grid (Smith et al. 2008).

2.3 Analysis methods

2.3.1 Fingerprint analysis

The preindustrial control runs show long-term drifts. It is assumed that the drifts are largely a result of the models not being in equilibrium with the control run forcing. Therefore, we remove the drifts by subtracting the linear trends at each model grid point separately. To compute fingerprints from the ensemble means of the ALL, GHG, ANT, NAT and AER runs and to estimate the background noise of internally-generated variability from the INT, we first regrid all 16 model outputs to a common 5° × 5° latitude/longitude grid by a bilinear interpolation and then convert the monthly outputs to annual products for the period 1900–2005. Regridding to a comparatively coarse resolution grid can weaken the spatial dimensionality of the datasets used, which is conducive to the estimation of the empirical orthogonal functions (EOFs) in the fingerprint analysis (Santer et al. 2007). Considering that model inconsistencies may affect the results, the multi-model ensemble

Table 2 Salient features of preindustrial control integrations used in this study

No.	Model	CTL_1	CTL_2	L
1	bcc-csm1-1	1	500	500
2	BNU-ESM	1450	2008	559
3	CCSM4	250	1300	1051
4	CanESM2	2015	3010	996
5	CNRM-CM5	1850	2699	850
6	CSIRO-Mk3-6-0	1	500	500
7	GFDL-CM3	1	500	500
8	GFDL-ESM2 M	1	500	500
9	GISS-E2-H	2410	2949	540
10	GISS-E2-R	3981	4530	550
11	IPSL-CM5A-LR	1800	2799	1000
12	IPSL-CM5A-MR	1800	2099	300
13	MIROC-ESM	1800	2330	531
14	MIROC-ESM-CHEM	1846	2100	255
15	MRI-CGCM3	1851	2350	500
16	NorESM1-M	700	1200	501
	Total	–	–	9633

CTL_1, CTL_2, and L denote (respectively) the first year, last year and length (years) of preindustrial control runs for calculating the sampling distributions of internally-generated variability shown in Fig. 4. Note that the start date of individual control runs is random

mean approach is used with the same weight for each model, despite of the number of ensemble realizations. The observational data is also transformed to the same 5° × 5° latitude/longitude target grid.

Let $S(t, i, j)$ signify annual mean SST data at time t from the ith realization of the jth model's runs. Data are expressed as anomalies relative to the period 1900–2005. The All ensemble averages ($S_{ALL}(t)$), GHG ensemble averages ($S_{GHG}(t)$), ANT ensemble averages ($S_{ANT}(t)$), NAT ensemble averages ($S_{NAT}(t)$) and AER ($S_{AER}(t)$) ensemble averages are calculated by first averaging each model's realizations (Table 1) and then averaging 16 different models. Finally, we calculate EOFs of the $S_{ALL}(t)$, $S_{GHG}(t)$, $S_{ANT}(t)$, $S_{NAT}(t)$ and $S_{AER}(t)$. The first EOF of each data set is simply defined as the fingerprint, for example, F_{ALL}, F_{GHG}, F_{ANT}, F_{NAT} and F_{AER}, which accounts for a massive fraction of the overall variance.

To estimate the background noise of internally-generated variability, two different data sets are typically required for the optimal fingerprint method used here. One data set is used to calculate the optimal fingerprint, and the second is employed to estimate the statistical significance of the fingerprint. Here, we first separate SST anomaly data from individual control run into two equal parts and then concatenate the first and the second from 16 control runs (Table 2), respectively. Finally, we obtain two noise data sets. For example, for the 16 different model control runs, we calculate anomalies for individual control run relative to its overall time span and then concatenate these anomalies to form two noise data sets $C_1(t)$ and $C_2(t)$. The index t indicates the concatenated time dimension. There are a total of time dimension of 4819 years of $C_1(t)$ and 4814 years of $C_2(t)$.

To assess the sensitivity of our results to the choice of fingerprint and noise, we further compute the signal-to-noise ratio (*S/N*). We perform the rotation of the fingerprint in the subspace of the first m EOFs of $C_1(t)$ or $C_2(t)$, where m denotes the alleged "truncation dimension." Here, we use the choice of m (=15) to rotate away from high noise directions and obtain the optimized fingerprint F^*. Furthermore, to reduce the artificial skill, the same noise data $C_1(t)$ or $C_2(t)$ is never contemporaneously used to optimize the fingerprint and estimate the signal-free time series $N(t)$ (Santer et al. 1995). Full details of the detection method are as follows.

We first calculate detection time series. Observational data $O(t)$ are expressed as anomalies relative to climatological mean for the entire period 1900–2005. Observed data $O(t)$ and noise data set $C_1(t)$ or $C_2(t)$ are projected onto the optimized fingerprint F^*, yielding a statistical time series $Z(t)$ and a signal-free time series $N(t)$, respectively. Then $Z(t)$ is fitted to the least-squares linear trends of increasing length L and compared with the standard error of the distribution of non-overlapping L length trends in $N(t)$. Here, we assume a Gaussian distribution of trends in $N(t)$ and use one-tailed Student t test. When the *S/N* exceeds above the 95 % confidence level, the detection is stipulated to occur and the results are in this sense statistically significant.

2.3.2 Heat budget analysis

We assume that SST can represent the mixed-layer mean temperature and therefore we can employ mixed-layer heat budget analysis to diagnose the formation of SST warming pattern. When the ocean temperature is integrated from the surface to the bottom of the mixed layer, the SST tendency can be expressed as:

$$C\frac{\partial T'}{\partial t} = D_o + Q_{net}, \tag{1}$$

where T' is SST change, $C = c_p^o \rho_o H$ is the heat capacity of the mixed layer, c_p^o is the specific heat at constant pressure, ρ_o is the density of seawater, H signifies the depth of the mixed layer, D_o denotes the ocean heat transport effect due to three-dimensional advection, mixing and even entrainment, Q_{net} indicates the change in the net surface heat flux into the ocean.

Since our study is mainly concentrated on the long-term variability of SST warming pattern, the 11-year running

mean is applied to suppress inter-annual variability. Given the inter-decadal and even longer time scales, spatial variations in the net surface flux and the ocean transport effect are one order of magnitude larger compared with SST tendency (Schneider and Fan 2012). Thus, D_o counteracts the change in Q_{net} to the first order,

$$0 = D_o + Q_{net}. \tag{2}$$

Considering the convenient diagnostic relationship used here, D_o is simply inferred without definitely estimating all of the advection, mixing and entrainment terms. Although some important ocean processes such as the deep water ventilation are missing in Eq. (2), they do not seem dominant in current study.

Surface heat flux is composed of four physical components: shortwave radiation Q_S, longwave radiation Q_L, turbulent fluxes of sensible heat Q_H and latent heat Q_E. Surface latent heat flux (Q_E) is often taken as a mixture of ocean response (Q_E^o) and atmospheric forcing (Q_E^a), but not as a single dynamic quantity (Xie et al. 2010a). In general, Q_E can be decomposed into a Newtonian cooling effect (Q_E^o) and a residual that represents atmospheric forcing (Q_E^a) due mostly to the atmospheric adjustments in wind speed, relative humidity and stability effects, which may not be directly tied to, but be quite influential in the formation of SST warming pattern. The first term can be casted as:

$$Q_E^o = \frac{\partial Q_E}{\partial T} T' = \alpha \bar{Q}_E T', \tag{3}$$

where $\bar{Q}_E$ denotes the climatological latent heat flux and α indicates the coefficient. The second term is calculated as:

$$Q_E^a = Q_E - Q_E^o. \tag{4}$$

Likewise, the wind speed effect (Q_E^w) can be obtained,

$$Q_E^w = \frac{\partial Q_E}{\partial W} W' = \frac{\bar{Q}_E W'}{\bar{W}}. \tag{5}$$

where W is surface wind speed, W' is surface wind speed change and $\bar{W}$ is the climatological surface wind speed.

In conclusion, SST warming pattern formation can be quantified by the following equation,

$$0 = D_o + Q_a - \alpha \bar{Q}_E T'. \tag{6}$$

The variations in SST warming are mainly attributable to ocean circulation variation (D_o), and atmospheric processes via radiative and turbulent fluxes ($Q_a = Q_S + Q_L - Q_H - Q_E$). Note that sensible heat flux ($Q_H = -c_p \rho_a C_H W S$, c_p is specific heat at constant pressure, ρ_a is surface air density, C_H is the transfer coefficient, W is surface wind speed, $S = T_a - T$ is surface stability parameter, T_a and T are total SST and surface air temperature at 2 m in kelvin) has been treated as a key component of atmospheric forcing (Q_a). Moreover, the SST dependency of surface evaporation may be regarded as a dominant damping to well balance forcing terms. The Newton cooling coefficient ($\alpha \bar{Q}_E$) acts as the ocean's ability of limiting the variations in SST warming via evaporation. Also, according to the Clausius–Clapeyron equation, the coefficient α can be calculated as $L R_v^{-1} T^{-2} \cong 0.06\ K^{-1}$. As noted in Xie et al. (2010a), α approximately equals to $0.06\ K^{-1}$.

3 Results

First, the temporal features of SST warming in the TIO are investigated. Then, we utilize an optimal detection method to optimize the fingerprint and further enhance the detectability of the fingerprint in observations (Gillett et al. 2002). The spatial characteristics of the TIO warming pattern are also examined. Finally, the relevant physical mechanisms responsible for the TIO warming pattern are given in details.

3.1 Temporal behavior of the TIO warming

Figure 1 illustrates the time evolutions of the TIO (20°S–20°N, 40°E–120°E) annual mean SST anomalies relative to the climatological mean over the entire period of 1900–2005 derived from observations and the ALL. For observations, HadISST and ERSST_V3b show a striking similarity in the basin-scale warming signal during 1900–2005, albeit some slight differences can also be found between two datasets, which are largely due to diverse resolutions and homogeneous methods in producing the data archives. It is clear that both the observations and ALL exhibit a rapid and non-monotonic warming since 1900, and the warming trend is approximately larger by a factor of 2 during 1965–2005 compared to the trend during 1900–1940. Here, the warming trend in the ALL is somewhat larger than that in observations. We suspect the underlying reason is that multi-model ensemble means of historical simulations reduce substantially intrinsic variability, whereas the observations still contain internally-generated variability. Besides, an inconsistency can be found between the observations and ALL during 1941–1964 (Fig. 1), which may be associated with multiple reasons (observational uncertainty and model internal variability, etc.). Therefore, for simplicity, we primarily focus on linear trend in variables during 1900–1940 and 1965–2005 in the following analyses.

To evaluate the performance of 16 CMIP5 models in simulating TIO SST non-uniform warming signal, we first compare multi-model ensemble means with the observations. Time series of annual-mean basin-scale SST anomalies in the TIO are shown in Fig. 2. It can be seen that the ALL, GHG and ANT capture the primary features of the TIO non-uniform warming observed since

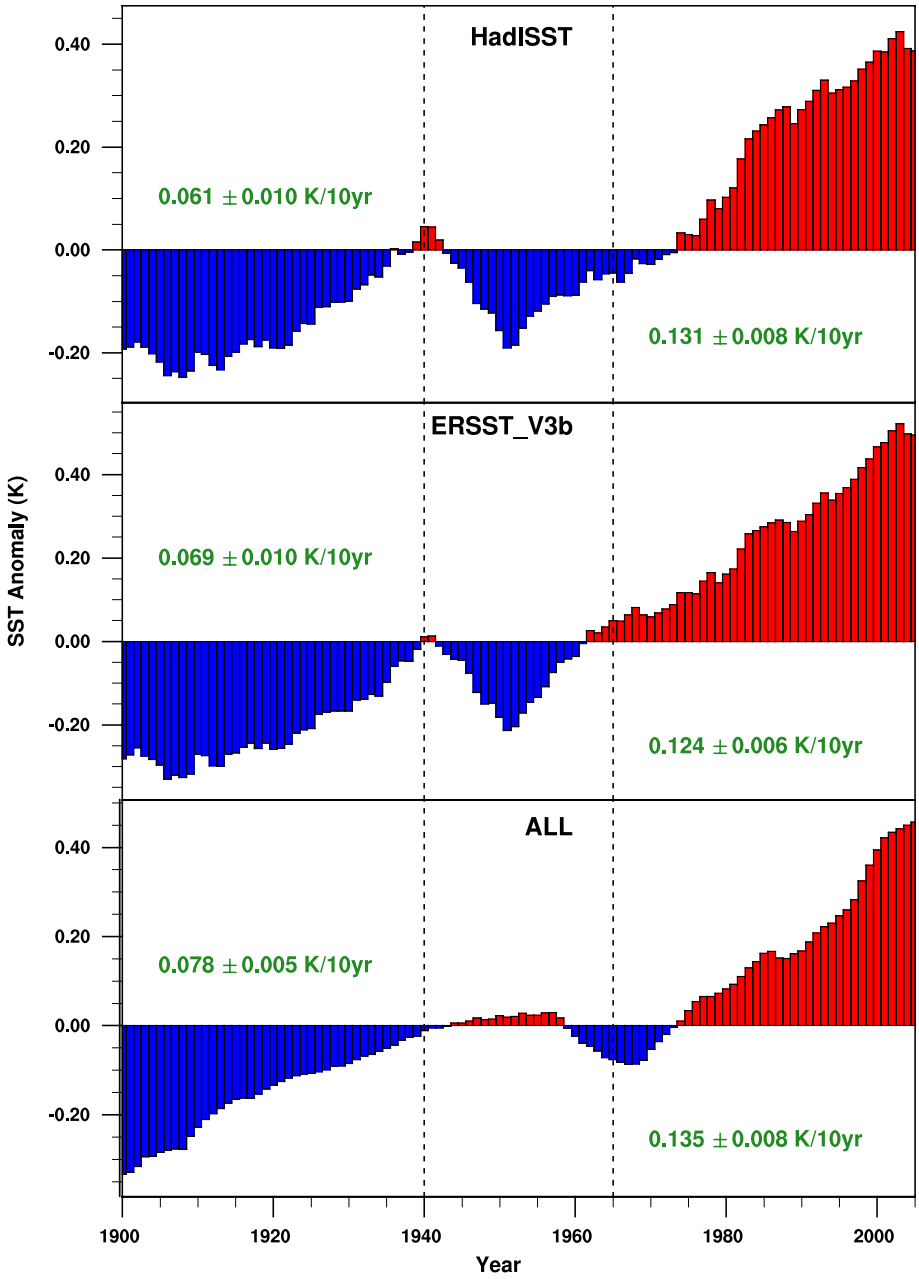

Fig. 1 Time series of annual mean SST anomalies over the TIO (20°S–20°N, 40°E–120°E) separately from the observations and ALL. The two numbers of each figure (respectively) indicate linear trend values plus/minus 95 % confidence limits according to the one-tailed Student *t* test during 1900–1940 and 1965–2005. The *black dashed lines* are shown to mark the transformation around 1940 and 1965. Units: *K*

1900. Specifically, both the ALL and observations exhibit a similar but not monotonous rate of warming during 1900–1940 and 1965–2005. The observed warming rate of about 0.06 K/decade during 1900–1940 is reproduced by the GHG, although the warming trend is overestimated since 1965. The ANT, however, underestimates the basin-scale warming trend. Additionally, the NAT displays an appreciable warming during 1900–1940 while such feature does not occur after 1965. The AER shows a significant cooling since 1900. In short, above results indicate that the observed warming is comparable with the forcing and response hypotheses embodied by the forced runs from the available 16 CMIP5 models ensemble.

For consistency when comparing forced responses and internal variability, we limit the length of piControl simulations examined to that of the shortest piControl runs, 255 years and then calculate the multi-model ensemble means. We further quantify the relative contributions of each forced run and internally-generated variability to the basin-scale warming in the TIO during 1900–1940 and 1965–2005 (Fig. 3). During 1900–1940, the observed warming trends of 0.061 ± 0.01 (0.069 ± 0.01) K/decade for HadISST (ERSST_V3b) are well captured by the ALL of 0.078 ± 0.005 K/decade (Fig. 3a). Under the ANT and NAT, the warming trend separately amounts to 0.037 ± 0.002 and 0.042 ± 0.005 K/decade, which

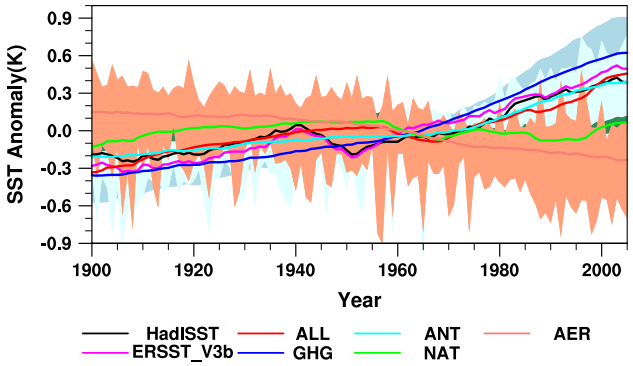

Fig. 2 Time series of the TIO annual mean SST anomalies for HadISST, ERSST_V3b, ALL, GHG, ANT, NAT and AER. *Black* and *magenta curves* denote HadISST and ERSST_V3b, respectively. *Red curve* is ensemble means of the ALL runs from 16 CMIP5 models. Similarly, *blue curve* is the GHG. *Cyan curve* is the ANT. *Green curve* is the NAT and *salmon curve* is the AER. The different models used here are weighted equally for ensemble means, despite the number of ensemble members they have. The *shaded regions* indicate the 5–95 % range of the distribution of SST anomalies obtained from the 16 CMIP5 models for the ALL, GHG, ANT, NAT and AER, respectively, which reflect uncertainty. Units: *K*

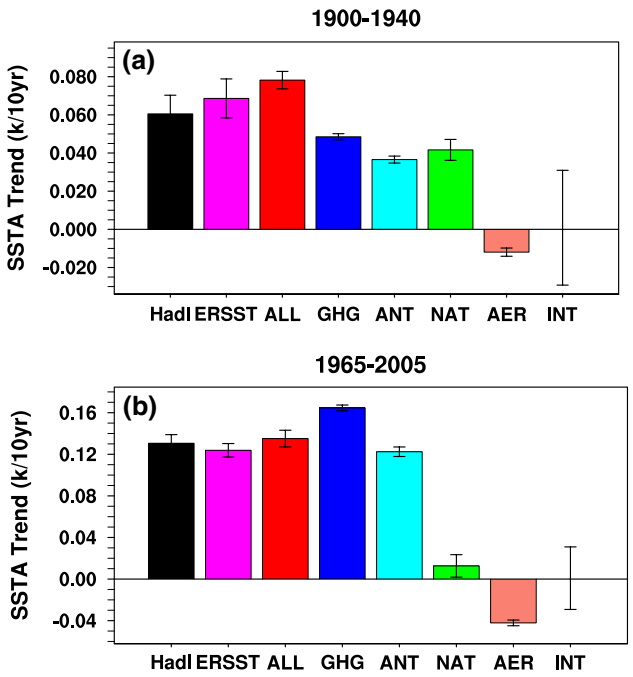

Fig. 3 The linear trends in the TIO basin-mean SST anomalies for HadI (HadISST), ERSST (ERSST_V3b), ALL, GHG, ANT, NAT, and AER during **a** 1900–1940 and **b** 1965–2005. The *whiskers* exhibit the linear trend values plus/minus 95 % confidence intervals according to the one-tailed Student *t* test. The INT represents assessed likely range of internal variability taken from the estimate of the 5th to 95th percentiles of non-overlapping 10-year linear trends of the first 255 years of multi-model ensemble means of preindustrial control runs. Units: *K/decade*

respectively account for approximately 50 % of the warming of the ALL. The GHG of 0.049 ± 0.002 K/decade implies that about one-fourth of the GHG-caused warming is offset by the AER of −0.012 ± 0.002 K/decade. The INT likely contributes to −0.29 to 0.03 K/decade. Above results reveal that the combined effect of GHGs and natural forcing may have contributed significantly to the observed warming during 1900–1940. During 1965–2005, the ALL of 0.135 ± 0.008 K/decade nearly equals to the warming trends of 0.131 ± 0.008 (0.124 ± 0.006) K/decade for HadISST (ERSST_V3b) (Fig. 3b). It is noteworthy that the ANT of 0.122 ± 0.005 K/decade contributes substantial warming trend of the ALL. Given the error bar, there is no significant warming trend in the NAT. The cooling trend induced by the AER is −0.04 ± 0.003 K/decade, offsetting roughly one-fourth of GHG-caused warming of 0.165 ± 0.003 K/decade. As for the internally-generated variability, it makes little contribution to the observed warming during 1965–2005. Therefore, we conclude that anthropogenic forcing has played a dominant role in the robust warming observed during 1965–2005. It is however noted that the ALL overestimates the observed 1900–1940 and 1965–2005 trends by at least 0.01 K/decade. This could mean that, besides external forcing, internal variability may also have an important role in contributing to the observed SST warming trends in the TIO (Roxy et al. 2014).

The general temporal features shown in multi-model ensemble means of Fig. 3 are also presented in many individual models (Fig. 4). Comparison of the multi-model ensemble means with individual models reveals that inter-models variations do not distort the consistency of the results during 1900–1940 (Fig. 4a–e) and 1965–2005 (Fig. 4g–k). Meanwhile, the warming trends of individual models indicate a relatively good agreement with observations in the overall temporal structure of the TIO warming. On the other hand, internal variability is likely to play a larger role in the observed SST warming during 1900–1940: approximately 29 % (115 of 400) of the unforced trends exceed the observed trends (Fig. 4f), compared to about 6 % (25 of 400) exceeding observations during 1965–2005 (Fig. 4l), as noted in Fig. 3. These results give us some confidence in the ability of 16 CMIP5 models to simulate the basin-scale characteristics of multi-decadal variability in the TIO SST.

3.2 Spatial pattern of the TIO warming

In this section, we use multi-model ensemble means to evaluate the TIO response to an imposed forcing change (fingerprint) and the background noise of natural climate variability (Barnett et al. 2005). A standard optimal detection method, as applied by Gillett et al. (2002), is utilized to

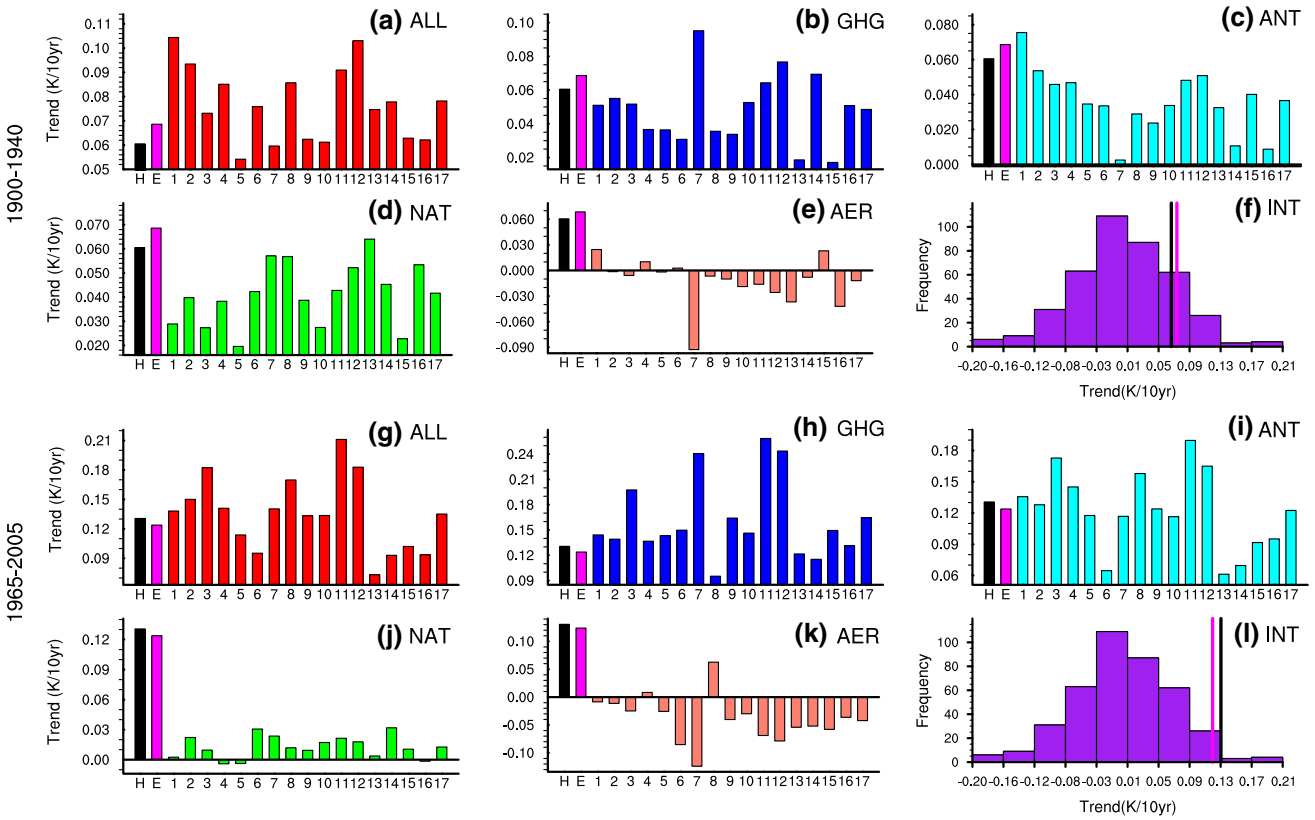

Fig. 4 Comparison of the observed (H-HadISST and E-ERSST_V3b) with modeled trends from ALL (**a**), GHG (**b**), ANT (**c**), NAT (**d**), AER (**e**) during 1900–1940 and ALL (**g**), GHG (**h**), ANT (**i**), NAT (**j**), AER (**k**) during 1965–2005 from 16 CMIP5 models as shown in Table 1 and the multi-model ensemble means (number 17). The sample distributions of non-overlapping 10-year linear trends from the first 255 years of each model's piControl run as shown in Table 2 are calculated (**f** and **l**). **f** *Black* and *red lines* denote the observed trends during 1900–1940 for HadISST and ERSST_V3b. **l** Same as **f** but for 1965–2005. Units: *K/decade*

estimate the fingerprint and noise modes by pooling information from multi-model ensemble means. This method has been extensively employed in studies of the height of the tropopause (Santer et al. 2004), near-surface temperature trend caused by GHG (Hegerl et al. 1996), surface temperature (Karoly and Wu 2005; Knutson et al. 1999; Stott 2003) and surface air temperature (Wu and Karoly 2007). Here, considering the limited length of observed instrumental record, we employ spatial optimization only.

We obtain the fingerprints estimated separately from the ALL, GHG, ANT, NAT and AER. The fingerprints are the first EOFs of the TIO SST anomalies during 1900–1940 (Fig. 5) and 1965–2005 (Fig. 6). During 1900–1940, the observations show large anomalous warming trend over most parts of the northwestern or western TIO and relatively weak warming in the southeastern TIO (Fig. 5a and b). Very similar SST distributions are seen in the GHG and NAT fingerprints (Fig. 5d and f). Particularly, both fingerprints explain a substantial fraction of the overall variance (about 96.2 and 94.3 %, respectively). The spatial pattern correlation coefficients between the observed warming trends and the GHG, NAT fingerprints are also very high (all exceeding 0.82; Fig. 5d and f). The spatial pattern is commonly referred to as a double-peak warming pattern. The ALL fingerprint primarily reflects a basin-scale warming (Fig. 5c) with explained variance of about 98.7 % and high spatial pattern correlation coefficients of exceeding 0.84, which is much stronger than the ANT fingerprint with slight warming (Fig. 5e). By comparison, the AER fingerprint shows general cooling trend with smaller explained variances and negative spatial pattern correlation coefficients of less than −0.67 (Fig. 5g). The leading noise mode primarily captures the cooling effect of SST variability over the TIO with negative spatial pattern correlation (Fig. 5h). We should note, however, that there exist some differences between the observed and the ALL, which may be due to the deficiencies of CMIP5 models (intrinsic variability simulation and responses to external forcing), the specified historical externally-forced factors and observational uncertainty. A certain fraction of area with inconsistent results are expected to occur (Knutson et al. 1999). Therefore, to a certain extent, we can still interpret the observed warming

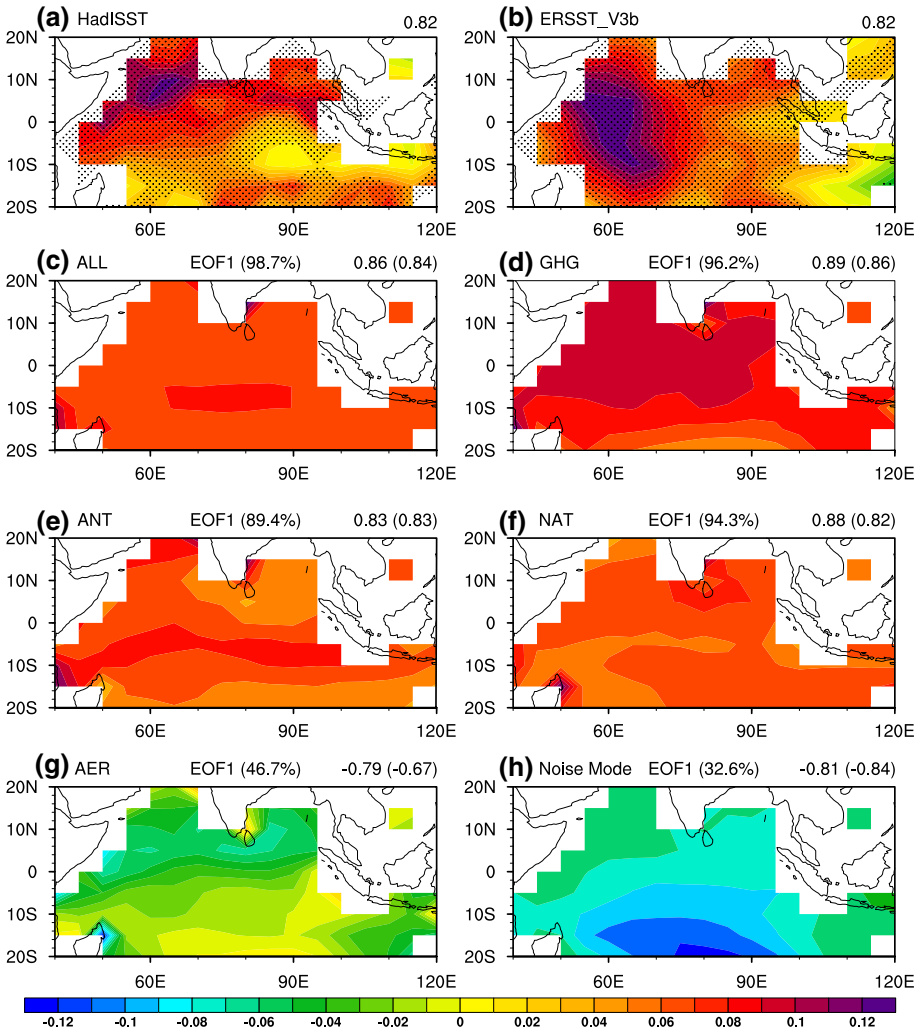

Fig. 5 Observed and simulated spatial patterns of variations in the TIO SST anomalies. The observed trends during 1900–1940 are shown in **a** (HadISST) and **b** (ERSST_V3b). The *dotted areas* are stipulated to be statistically significant at the 95 % confidence level. The fingerprints for ALL (**c**), GHG (**d**), ANT (**e**), NAT (**f**) and AER (**g**) are shown. Also shown is the leading noise mode of the concatenated INT ($C_1(t)$) runs (**h**). The numbers at the *top-right above each panel* indicate spatial pattern correlation coefficients between HadISST and ERSST_V3b (**a** and **b**), the fingerprints and the observed trends (**c**–**h**). Percentage explains variance contribution for each fingerprint and noise mode

trends as attributable to GHGs and natural forcing. Our study provides compelling evidence that the double-peak warming pattern can be well explained by a combination of warming largely due to increase in well-mixed greenhouse gases, and natural forcing, with some cooling at least in part due to aerosols, and substantial, but not implausible, contribution from internally-generated variability.

During 1965–2005, the observed warming trends (Fig. 6a and b) and the ANT fingerprint (Fig. 6e) exhibit a robust basin-scale warming pattern of the same polarity with a pronounced geographic distribution (termed as a non-uniform IOBM-like warming pattern) covering the whole TIO basin (Du et al. 2013). The ANT fingerprint explains a considerable fraction of the overall variance (98.6 %) with very high pattern correlation coefficients of exceeding 0.94. It corresponds more closely to the ALL fingerprint (Fig. 6c) than to the GHG fingerprint (Fig. 6d). The NAT fingerprint shows anomalous warming with a stronger magnitude in the northern TIO (Fig. 6f). The AER fingerprint (Fig. 6g) exhibits stronger cooling over the northern TIO than that over the southern TIO, to a large extent, because of stronger aerosol (Barnett et al. 2005) and the rapid growth of aerosol concentrations after the 1950s (Xie et al. 2013). It explains a substantial fraction of the overall variance (approximately 87.8 %) but with smaller negative correlation coefficients (less than −0.84; Fig. 6g). Additionally, the noise has relatively low loadings but with high spatial correlation coefficients (Fig. 6h). These results lend credence to the view that the non-uniform IOBM-like warming pattern is largely caused by changes in anthropogenic forcing.

To explore the sensitivity of the results obtained from the optimal detection method, we show the estimations of signal-to-noise ratio (S/N) during 1900–1940 and 1965–2005 in Fig. 7. Despite the short model simulation length during 1900–1940, the GHG and NAT signals are consistently detectable and both show a smooth increase (Fig. 7a). As the trend interval L increases, there occurs a pronounced decrease in the standard error of the sampling distributions of trends in noise (Fig. 7c). The remarkable increase in the

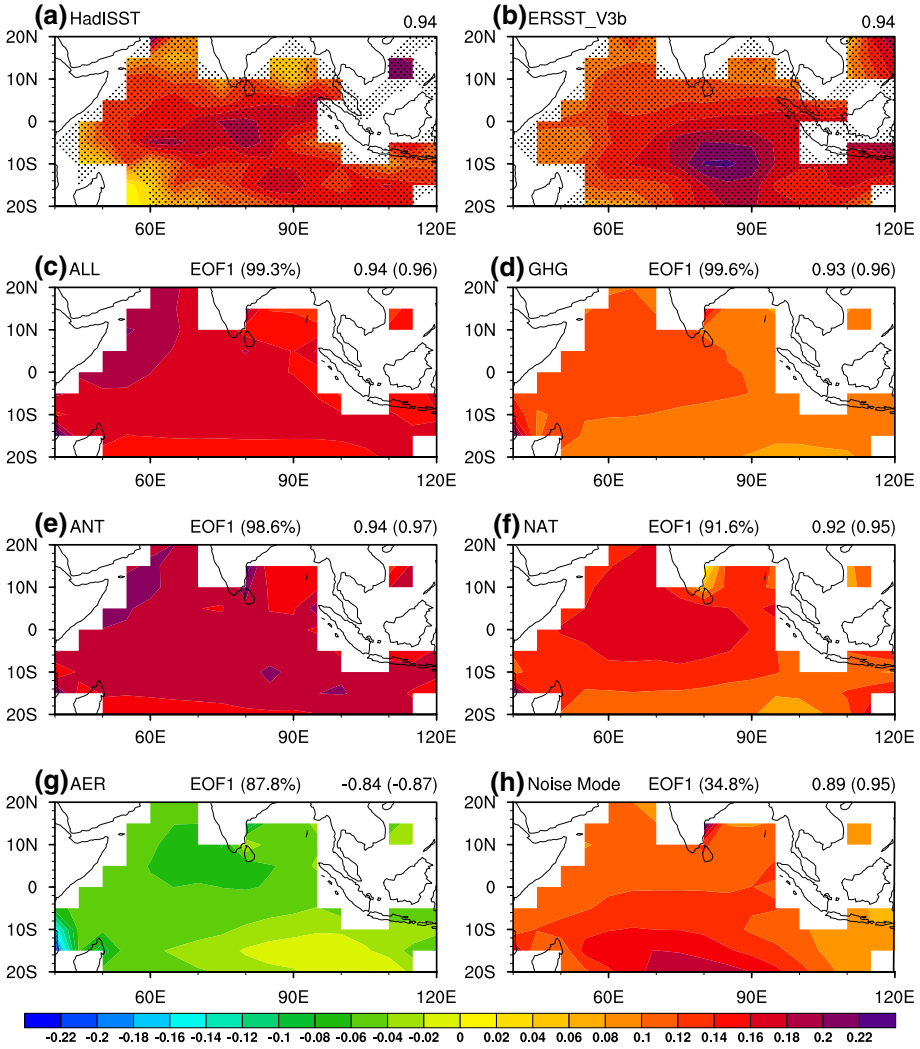

Fig. 6 Same as in Fig. 5 but for 1965–2005. Note that **h** the leading noise mode of the concatenated INT ($C_2(t)$) is calculated

S/N plotted in Fig. 7e arises mainly from the decrease in the standard error of the noise with increasing trend length. During 1965–2005, there is a gradual increase in the ANT signal with the trend interval L increasing (Fig. 7b). The rapid decrease in the standard error of the noise (Fig. 7d) may be due not only to an obvious decrease in noise amplitude with longer trend interval L, but also largely to dissimilarity between the ANT fingerprint pattern and the pattern of noise in $C_1(t)$, which results in a progressive growth in S/N (Fig. 7f). To some extent, these underscore the credibility of our results in Figs. 5 and 6.

3.3 Physical mechanisms for the double-peak and non-uniform IOBM-like warming pattern

We further determine the relevant causes of the formation of the double-peak and inhomogeneous IOBM-like warming pattern in the TIO based on the mixed-layer heat budget analysis. Here, we primarily focus on evaluating the response to the all-forcing from 16 CMIP5 models ensemble means, which has important implications for detecting the key physical mechanisms responsible for the TIO inhomogeneous warming patterns. In consideration of the credibility and physical consistency between the observed and model simulations, we also examine the role of the combined effects of the GHG and the NAT during 1900–1940, and the ANT during 1965–2005 in forming the TIO warming patterns.

Atmospheric and oceanic processes in the ALL are shown in Fig. 8. During 1900–1940, atmospheric processes via radiative and turbulent fluxes (Q_a) present two maximum centers: one appears in most parts of the northwestern basin and the other is located in the southeastern basin (Fig. 8a), resembling the double-peak structure in Fig. 5a. Ocean heat transport effect (Q_o) produces cooling trend off Java and Sumatra and over the northwestern TIO (Fig. 8c). Note that the sum of atmospheric and oceanic processes ($D_o + Q_a$) reveals a double-peak structure, with conspicuous warming located in the northwestern basin and stronger warming along 10°S–20°S (Fig. 8e), which

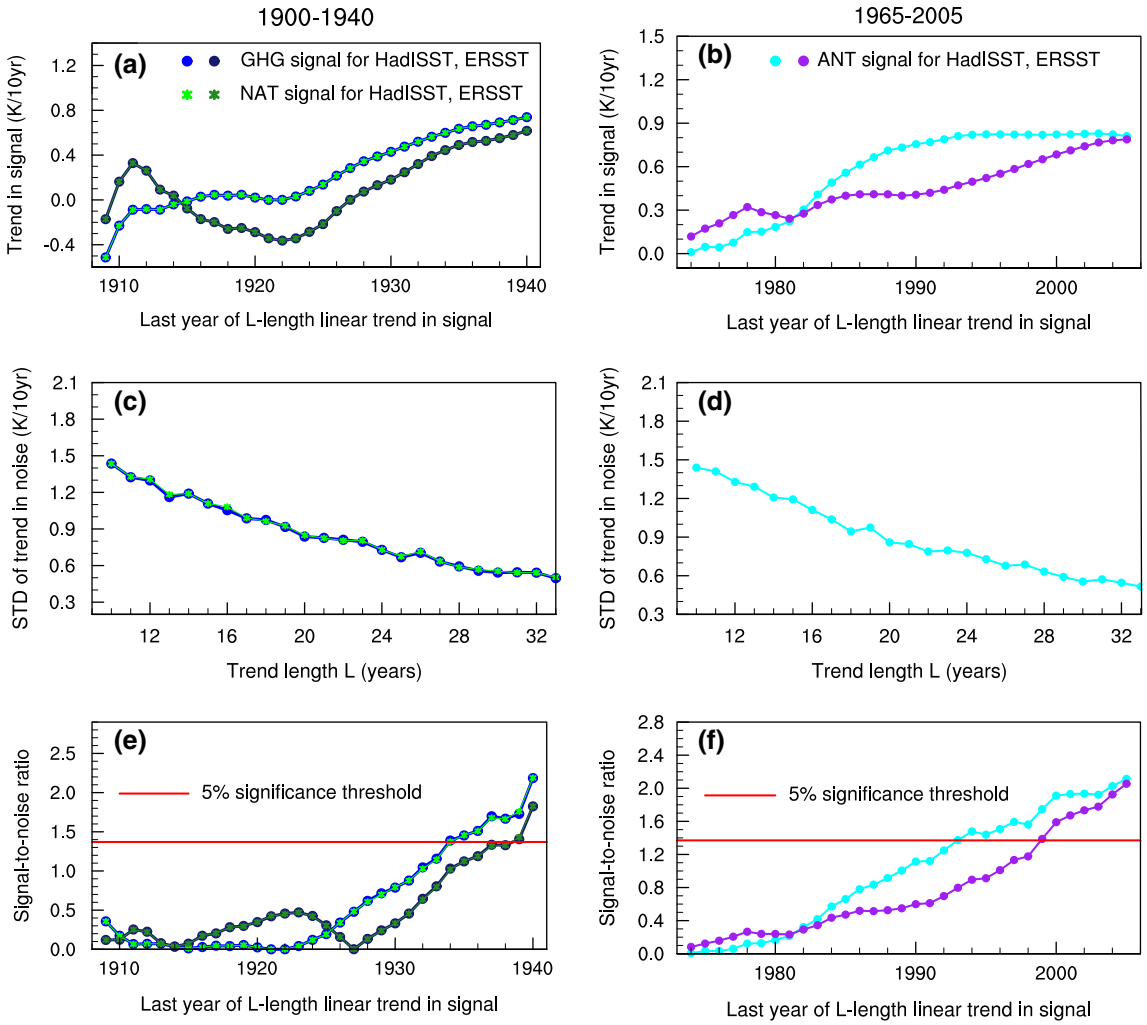

Fig. 7 The optimized GHG and NAT fingerprints (also termed as signal (**a**) and the noise (**c**) component of the signal-to-noise ratio (*S/N*, **e**) used for estimating the sensitivity of the results during 1900–1940 are fully illustrated. The ANT signal (**b**) and the noise (**d**) component of the *S/N* (**f**) during 1965–2005 are also clearly listed. Note that two observational data sets are projected onto the optimized fingerprints to obtain two signals, for example the cyan and purple lines for HadISST and ERSST (**b**). The *horizontal red lines* (**e** and **f**) are the stipulated 5 % significance thresholds for a one-tailed Student *t* test, assuming a Gaussian distribution of noise trends

largely contributes to the formation of the double-peak warming pattern. In addition, spatial pattern correlation coefficient between the sum of atmospheric processes and ocean heat transport ($D_o + Q_a$), and the observed warming trend amounts to 0.84 (0.82) for HadISST (ERSST_V3b). The distribution of the Newtonian cooling coefficient $\alpha\bar{Q}_E$ affects the variations in SST warming (Fig. 8g) and hence the variations in climatological latent heat flux ($\bar{Q}_E$) is very important for the double-peak pattern formation, as indicated in Eq. (6). It is clear that the combined effects of atmospheric and oceanic processes play a key role in the formation of the double-peak warming pattern. During 1965–2005, atmospheric processes (Q_a) almost warm the entire basin but with remarkable sub-basin variations (Fig. 8b), which are in favor of the formation of the non-uniform IOBM-like warming pattern, though with pronounced cooling induced by ocean heat transport effect in the eastern TIO (Fig. 8d). The sub-basin variations in Q_a may be largely due to the buildup of aerosols in the northern TIO compared to that in the southern TIO (Barnett et al. 2005), which weakens the SST warming signal, as shown in Fig. 6g. The sum of atmospheric processes and ocean circulation change ($D_o + Q_a$) displays the basin-wide warming effect (Fig. 8f), similar to the climatological latent heat flux (Fig. 8h), which is favorable for the inhomogeneous IOBM-like warming pattern formation. Furthermore, spatial pattern correlation correlations between the sum of atmospheric processes and ocean circulation change, and the observed trends (HadISST and ERSST_V3b) are approximately 0.92 and 0.96. These results imply that we

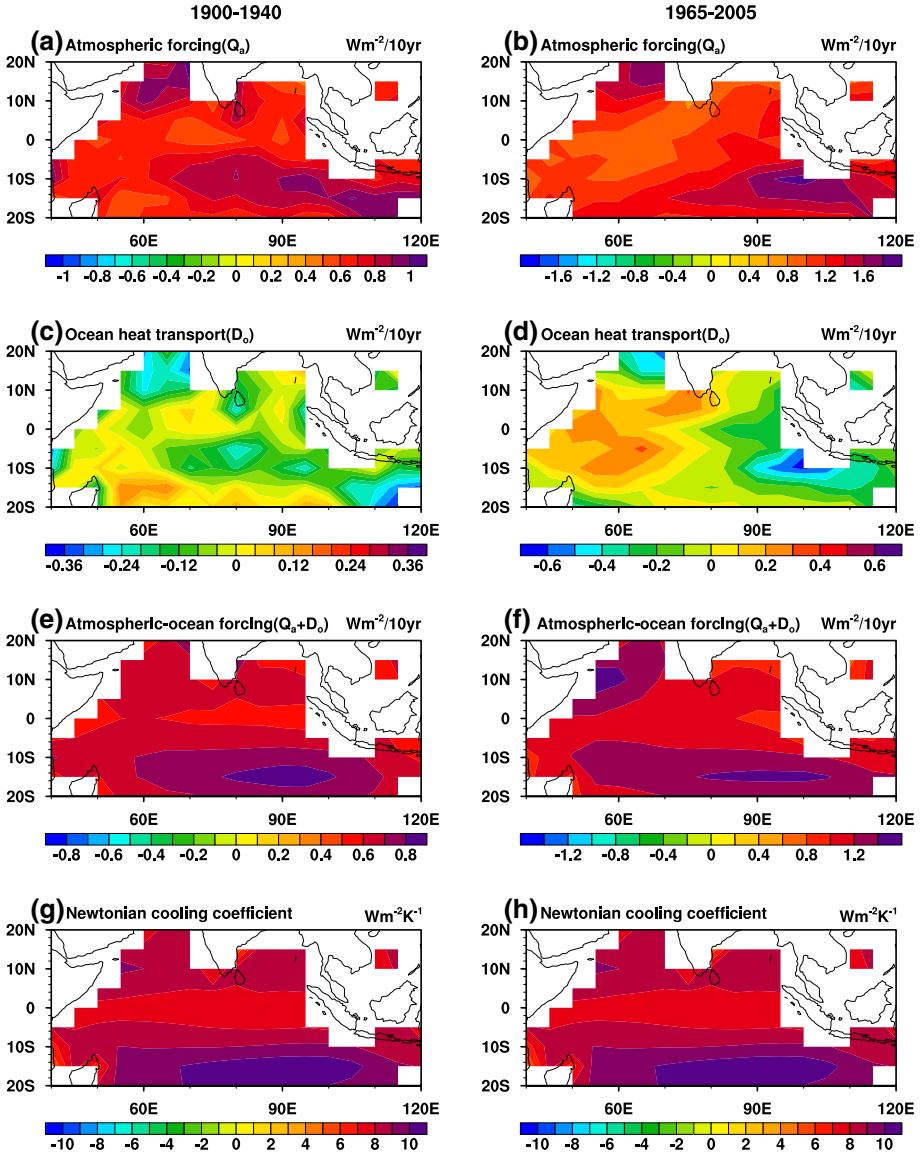

Fig. 8 The linear trend of **a** atmospheric processes via radiative and turbulent fluxes (Q_a), **c** ocean heat transport effect (D_o), **e** the sum of atmospheric and oceanic processes ($Q_a + D_o$) from ensemble means of the all-forcing runs from 16 CMIP5 models during 1900–1940 in the TIO. **b**, **d** and **f** are the same as **a**, **c** and **e** but for 1965–2005, respectively. **g** The Newtonian cooling coefficient ($\alpha\bar{Q}_E$, units: $\mathrm{Wm^{-2}K^{-1}}$) is the same as **h**. Our convention for warming ocean is positive. Units: $\mathrm{Wm^{-2}}$/10 yr

can interpret the double-peak and non-uniform IOBM-like pattern as attributable, at least in a large part, to the sum of atmospheric processes and ocean circulation change.

Besides, we also examine four physical components of atmospheric processes (Q_a), such as surface shortwave radiation (Q_S), surface longwave radiation (Q_L), sensible heat flux (Q_H), and latent heat flux from atmospheric forcing (Q_E^a). Surface shortwave radiation (Q_S) shows weak warming in the whole basin except some patched areas where slight cooling occurs during 1900–1940 (Fig. 9a). In contrast, there is a widespread cooling in the almost entire basin except some warming patched areas during 1965–2005 (Fig. 9b) owing primarily to intensified water vapor absorption caused by the lower troposphere moistening (Trenberth and Fasullo 2009). The increase in convective clouds due chiefly to increased SST in the TIO reduces shortwave radiation even more. Downward longwave radiation nearly warms all the basin but with a stronger magnitude during 1900–1940 (Fig. 9c) in contrast to the warming during 1965–2005 (Fig. 9d) because of increased GHG forcing and enhanced water vapor feedback (Du and Xie 2008). Sensible heat flux also warms the entire basin, albeit with a reduced magnitude (Fig. 9e and f). It should be noted that latent heat fluxes from atmospheric forcing part (Q_E^a) with a larger magnitude (Fig. 9g and h) show similar spatial patterns to the sum of atmospheric and oceanic processes, which indicates that Q_E^a can be considered as the dominant mechanism for the TIO warming and can imprint strongly on the SST warming. Our study confirms that Q_E^a plays a key role in causing the double-peak and inhomogeneous IOBM-like warming pattern.

The wind effect on latent heat flux from atmospheric forcing part features two peaks located in the northwestern basin and along 0°–15°S (Fig. 10a) due to reduced

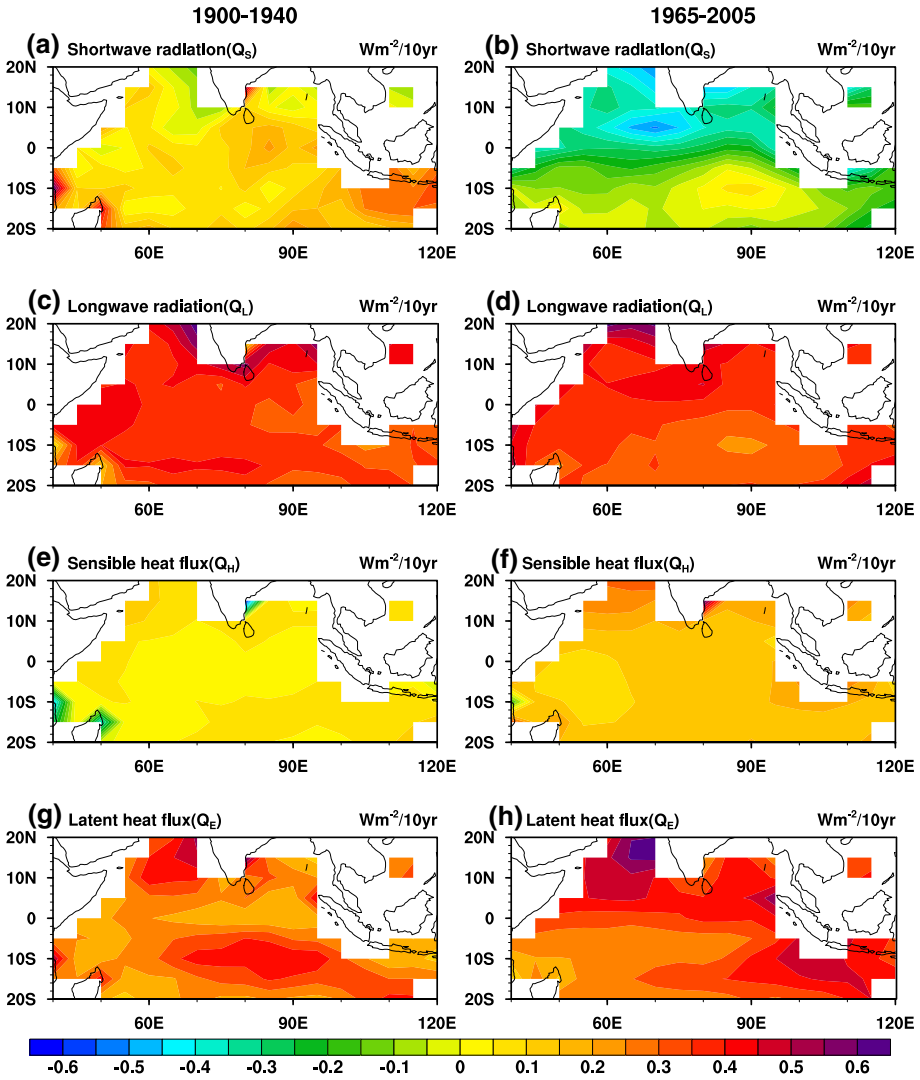

Fig. 9 The linear trend of **a** surface shortwave radiation (Q_S), **c** surface longwave radiation (Q_L), **e** sensible heat flux (Q_H), **g** latent heat flux from atmospheric forcing (Q_E^a) from ensemble means of the all-forcing runs from 16 CMIP5 models during 1900–1940 in the TIO. **b**, **d**, **f** and **h** are the same as (**a**), **c**, **e** and **g** but for 1965–2005, respectively. Our convention for warming ocean is positive. Units: Wm^{-2}/10 yr

climatological wind speed (Fig. 11a), nearly coincident with the double-peak warming pattern. The ALL captures the significant SST warming signal in observations, simultaneously with the weak anti-symmetric atmospheric circulation (Fig. 10c). Specifically, consistent with the robust SST warming (Fig. 10c) and intensified atmospheric convection (Fig. 10g), anomalous surface winds are characterized by an anti-symmetric wind pattern, with anomalous easterly north and northwesterly south of the equator. The northwesterly anomalies help to suppress the prevailing southeasterly over the southeastern TIO and the easterly anomalies reduce the climatological westerly over the northern TIO (Fig. 11a), which act to sustain the SST warming. Compared to climatological sea surface height (Fig. 11a), sea surface height anomaly exhibits two peaks located in the northwestern TIO and along 10°S, which helps to enhance thermocline feedback to reduce upwelling and raise SST in the south TIO (Huang and Kinter 2002). As identified in coupled general circulation model simulations (Du et al. 2009), the anti-symmetric atmospheric circulation is initiated by the down-welling Rossby wave-induced SST warming in the south TIO. The down-welling Rossby wave primarily reduces upwelling (Xie et al. 2002) and further anchors the anti-symmetric atmospheric circulation, suggestive of their mutual interaction. This conclusion needs to be further verified in models on multi-decadal time scales. These results suggest that the anti-symmetric wind anomalies maintain the warming over the northwestern and southeastern TIO. Our study also highlights that, to a certain extent, internal ocean–atmosphere interaction within the TIO is of vital importance to sustain the double-peak warming pattern.

During 1965–2005, the wind effect on latent heat flux from atmospheric forcing part almost warms the entire basin but with stronger magnitude (Fig. 10b) compared to that during 1900–1940 (Fig. 10a), which may be associated with reduced climatological surface wind (Fig. 11b). The non-uniform basin-scale warming is well reproduced

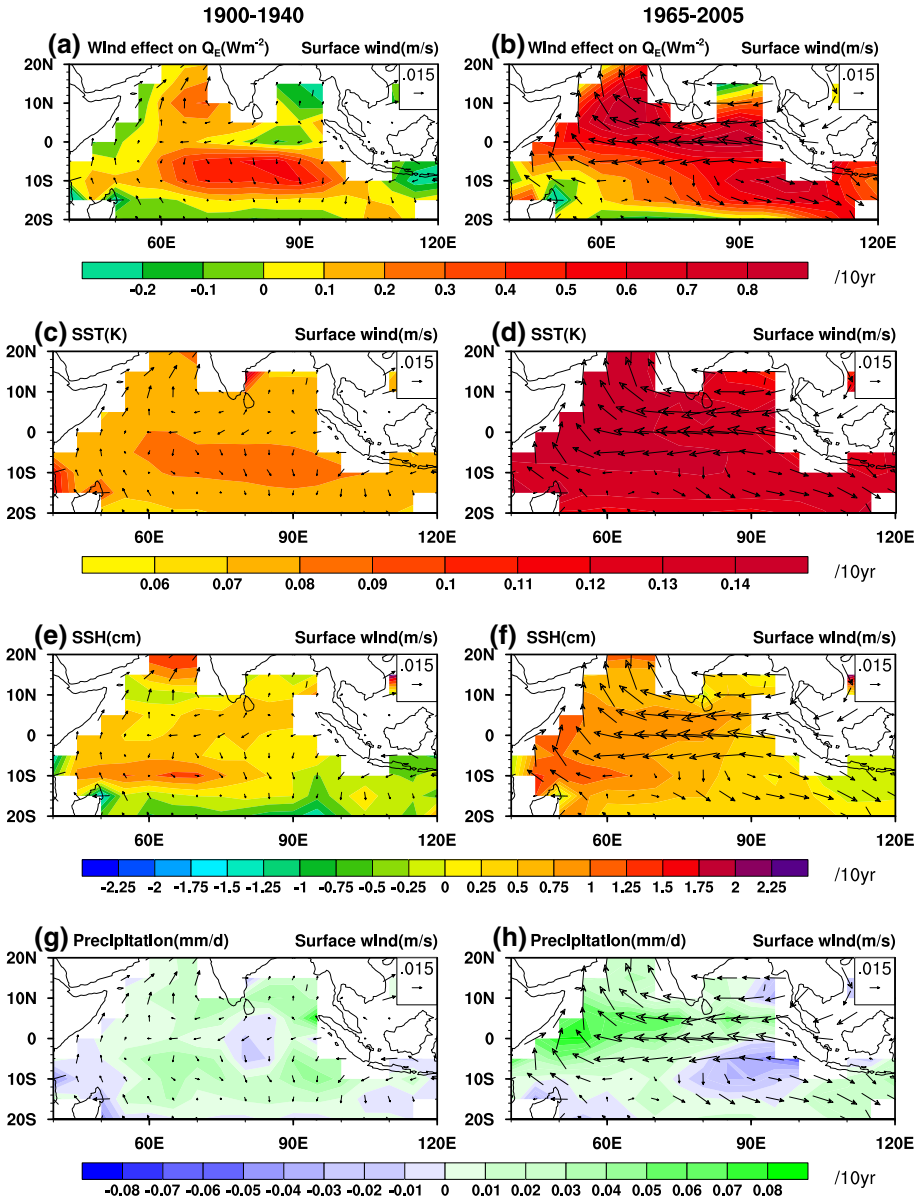

Fig. 10 The linear trend of **a** wind effect on latent heat flux from atmospheric forcing part (Q_E^W, *colors*, Wm^{-2}/10 yr) and surface wind (vector, ms^{-1}/10 yr), **c** SST (*colors*, K/10 yr) and surface wind (vector, ms^{-1}/10 yr), **e** sea surface height (SSH, *colors*, cm/10 yr) and surface wind (vector, ms^{-1}/10 yr), and **g** precipitation (*colors*, mmd^{-1}/10 yr) and surface wind (vector, ms^{-1}/10 yr) from ensemble means of the all-forcing runs from 16 CMIP5 models during 1900–1940 in the TIO. **b**, **d**, **f** and **h** are the same as (**a**), **c**, **e** and **g** but for 1965–2005, respectively

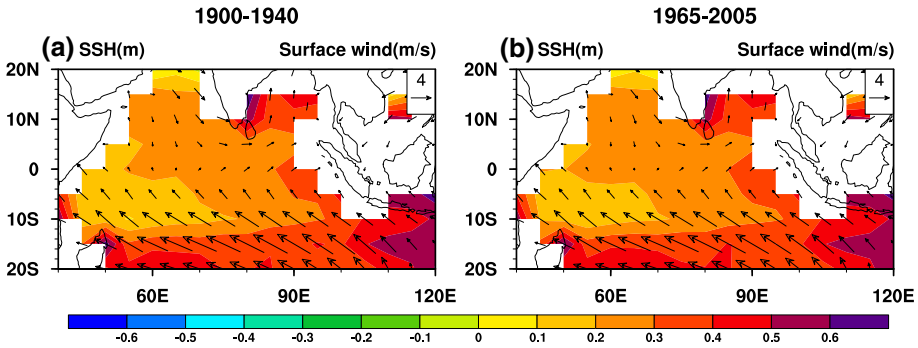

Fig. 11 Climatology of surface wind (vector, m/s) and sea surface height (SSH, *color*, m) for the ALL are shown in **a** 1900–1940 and **b** 1965–2005

by the ALL (Fig. 10d) with intensified anti-symmetric wind anomalies. The anti-symmetric wind pattern features reinforced easterly occupying most parts of the northern TIO and enhanced northwesterly extending over the southern TIO. Associated with the C-shaped wind pattern, the easterly anomalies weaken climatological westerly over

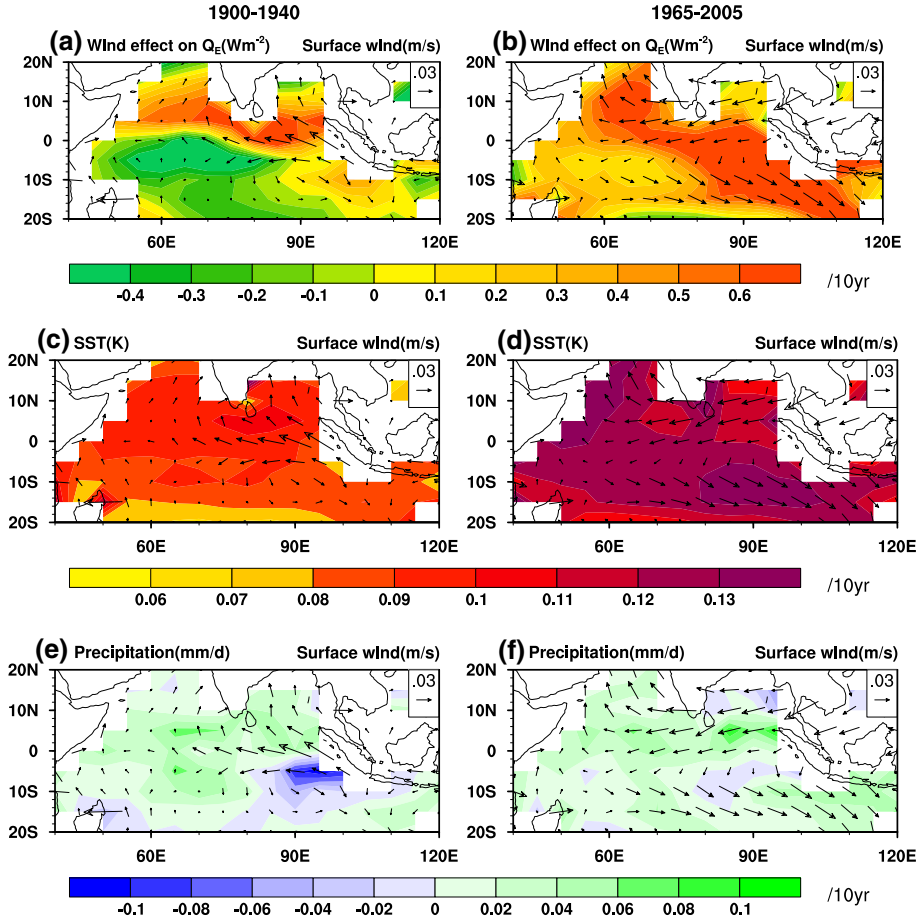

Fig. 12 The linear trend of **a** wind effect on latent heat flux from atmospheric forcing part (Q_E^W, *colors*, Wm^{-2}/10 yr) and surface wind (vector, ms^{-1}/10 yr), **c** SST (*colors*, K/10 yr) and surface wind (vector, ms^{-1}/10 yr) and **e** precipitation (*colors*, mmd^{-1}/10 yr) and surface wind (vector, ms^{-1}/10 yr) from ensemble means of the GHG-forcing-only and natural-forcing-only runs from 16 CMIP5 models during 1900–1940 in the TIO. **b**, **d** and **f** are the same as (**a**), **c** and **e** but for ensemble means of anthropogenic-forcing-only runs from the same 16 CMIP5 models during 1965–2005, respectively

the northern TIO and the northwesterly anomalies reduce the southeasterly trades over the southern TIO, which are favorable for the non-uniform IOBM-like warming pattern. As stated by Du et al. (2013), the anomalous SST warming over the south TIO induced by the down-welling ocean Rossby wave and enhanced atmospheric advection with positive precipitation anomalies (Fig. 10h), reflecting the slowdown of the Walker circulation under global warming (Tokinaga et al. 2012; Vecchi et al. 2006), trigger the anti-symmetric atmospheric circulation. Positive sea surface height anomalies deepen the thermocline and sustain the SST inhomogeneous warming pattern, indicative of sea surface height anomaly-thermocline depth anomalies (Fig. 10f). These results are indicative of local ocean–atmospheric interaction and ocean dynamic effect in the interior TIO, implying the importance for the non-uniform IOBM-like warming pattern formation.

The contributions of the combination of GHG and natural forcing during 1900–1940 and anthropogenic forcing during 1965–2005 to the TIO warming are further examined. The increase in longwave radiation and latent heat flux from atmospheric forcing part is primarily caused by the GHG (not shown). The variations in wind effect on latent heat flux exhibits two maximum centers located in the northern and southeastern TIO, which is at least in part favorable for the double-peak warming pattern, albeit with a smaller magnitude during 1900–1940 (Fig. 12a). During 1965–2005, it shows the inhomogeneous IOBM-like warming pattern (Fig. 12b). The anti-symmetric atmospheric circulation significantly enhances during 1900–1940 (Fig. 12c), with relatively large southwesterly north of the equator. The positive precipitation anomalies still exist (Fig. 12e), but with a magnitude smaller than that in the ALL. Note that the inhomogeneous IOBM-like warming with a larger magnitude is mainly attributable to the anthropogenic forcing during 1965–2005 (Fig. 12d), with the reinforced anti-symmetric wind anomalies. Consistent with the anti-symmetric circulation structure, the precipitation pattern is very similar to the ALL (Fig. 12f). Our results succeed in capturing salient spatio-temporal characteristics and crucial physical mechanisms for the double-peak and inhomogeneous IOBM-like warming pattern, which are separately induced by the combined effect of the GHG and NAT, and the ANT. We further demonstrate that internal ocean–atmosphere interaction and ocean dynamic processes within the TIO may be identified as the major physical causes of maintaining the TIO inhomogeneous warming.

4 Summary and discussion

4.1 Summary

We have carried out an investigation into the important physical mechanisms responsible for the TIO SST non-uniform warming during 1900–2005 by using the latest 16 CMIP5 models against observations. Our analysis is primarily based on ensemble means of multi-model simulations from six sets of experiments, including twentieth century historical runs, GHG-forcing-only runs, anthropogenic-forcing-only runs, natural-forcing-only runs, aerosol-forcing-only runs and preindustrial control runs. Again, an optimal detection method is applied to capture fingerprints in observations.

The TIO inhomogeneous warming exhibits considerable spatio-temporal features as follows. On multi-decadal time scales, the observed SST warming trend during 1965–2005 is approximately larger by a factor of 2 than that during 1900–1940. The warming trend during 1900–1940 is mainly attributable to the combined effect of GHG and natural forcing. During 1965–2005, anthropogenic forcing well captures the robust warming trend. On the other hand, the double-peak warming pattern with anomalous warming in the northwestern or western TIO and relatively weak warming in the southeastern TIO is the dominant mode of the TIO SST variability during 1900–1940. During 1965–2005, the observed warming trend exhibits a basin-wide warming pattern of the same polarity with a pronounced geographic distribution covering the entire TIO basin, which is generally referred to as the non-uniform IOBM-like warming pattern. The optimal detection analysis indicates that the double-peak warming pattern is mostly caused by the combined effect of GHGs and natural forcing, with some cooling owing to the aerosol forcing and substantial, but not implausible contribution from internally-generated variability. The inhomogeneous IOBM-like warming pattern is attributable, at least in a large part, to the anthropogenic forcing.

Moreover, the mixed-layer heat budget analysis demonstrates that both atmospheric processes via radiative and turbulent fluxes and oceanic processes are vital to the formation of the double-peak and non-uniform IOBM-like warming pattern, especially latent heat flux from atmospheric forcing part. The wind effect on latent heat flux is also very important for the SST inhomogeneous warming pattern formation. From an internal ocean–atmosphere interaction perspective of view, surface wind anomalies are characterized by the weak anti-symmetric atmospheric circulation during 1900–1940. The anti-symmetric wind pattern features weak easterly (northwesterly) anomalies north (south) of the equator, weakening climatological westerly wind (southeasterly trades) north (south) of the equator and helping to maintain the SST warming over the northwestern (southeastern) TIO, a key physical mechanism for sustaining the double-peak warming pattern. In comparison with the weak anti-symmetric wind pattern, the striking wind pattern occupies the entire basin during 1965–2005 due a large part to the anthropogenic forcing. The intensified anti-symmetric wind pattern reduces the climatological westerly wind (southeasterly trades) north (south) of the equator, which is in favor of the inhomogeneous IOBM-like warming pattern. Atmospheric GCM experiments have demonstrated that the anti-symmetric wind pattern is forced by robust SST warming and enhanced atmospheric convection over the south TIO, which in turn is sustained by the down-welling ocean Rossby waves. However, the conclusion needs to be further substantiated on multi-decadal time scales. Our results imply that intrinsic ocean–atmosphere interaction and ocean dynamic processes are the predominant physical mechanisms for maintaining the TIO inhomogeneous warming pattern (Du et al. 2009, 2013). The recognition of the internal ocean–atmosphere interplay and ocean dynamics has vital implications for future regional climate projection, calling for improved monitoring and modeling of the TIO SST warming.

4.2 Discussion

There are some caveats of our results. Although the ALL can simulate, at least in part, the spatio-temporal characteristic and relevant physical processes in the TIO, significant difference between the observations and models exists. The observed SST trend is relatively small along 5°S–10°S and increases southward to 15°S–20°S in the southern TIO (Fig. 5a, b), while the SST warming trend is larger along 5°S–10°S than that along 15°S–20°S in ALL (Fig. 5c). So, there appears to be a different N-S change in the trend between the observations and ALL. According to Fig. 8c, ocean heat transport (D_o) shows cooling trend along 5°S–10°S, consistent with the smaller SST warming trend in observations (Fig. 5a, b). In Fig. 8a, atmospheric forcing (Q_a) exhibits different feature with larger trend along 10–15S and decreasing southward and northward. Additionally, latent heat flux from atmospheric forcing part displays the largest trend along 10S (Fig. 9g), similar to the changes in the wind effect on latent heat flux of the atmospheric forcing part in ALL (Fig. 10a), which qualitatively accounts for larger warming trend along 5°S–10°S than that along 15°S–20°S (Figs. 5c, 10c). These results suggest that the difference between observations and the ALL is mainly caused by the wind effect on the atmospheric forcing part of latent heat flux. During 1900–1940, the relatively small easterly anomalies appear in the equatorial Indian Ocean, although the equatorial Indian Ocean SST warming trend is homogenous (Fig. 10c). The east–west SSH change

gradient is not also significant (Fig. 10e), which indicates that the thermocline response to the equatorial zonal wind anomaly isn't reproduced by the ALL. The easterly anomalies may cause more precipitation over the equatorial western Indian Ocean than that over the equatorial eastern Indian Ocean (Fig. 10g). It is indicated that the ALL produces the unrealistic Bjerknes feedback, primarily including the zonal wind response to SST anomaly. During 1965–2005, the easterly anomalies are larger along 5°S–20°N, but the SST warming trend shows the IOBM-like warming pattern with a large magnitude (Fig. 10d). The robust easterly anomalies also uplift the thermocline in the eastern basin (small SSH trend, Fig. 10f) and deepen the thermocline in the western basin (large SSH trend, Fig. 10f). Moreover, the more precipitation occurs in the western TIO than that in the eastern TIO (Fig. 10h). It is worth noting that the simulation of the Bjerknes feedback in the ALL is unrealistic especially with regard to the zonal wind response to SST anomaly over the TIO, as discussed in Liu et al. (2013). Therefore, we can also interpret the difference between the observations and ALL during 1900–1940 as attributable, at least in part, to model deficiencies, especially the unrealistic simulation of the Bjerknes feedback.

Although the components of the response to a wide range of different forcings are well established (Taylor et al. 2012), the real effect of different forcings is still uncertain because of the nonlinearity of the climate system. Here, a multi-model ensemble means approach is employed to reduce systematic errors of individual models and inter-model differences, and therefore make our results more authentic. Moreover, only finite realizations of a few models and a limited number of models that carried out necessary experiments are available, a fact that constrains the size of the multi-model ensemble. The use of as many CMIP5 models as possible in order to decrease model biases and obtain different combinations of forcings is of vital importance to quantify the TIO SST warming.

The physical causes of the TIO warming are still seen as a challenge for scientific communities. Concerning the accuracy and duration of different surface heat flux products, there occurs considerable uncertainty for the net heat flux as a significant cause for the TIO SST warming (Yu and Weller 2007). Ocean general circulation models even show a larger spread (Godfrey et al. 2007). With a substantial slowdown of the Indian Ocean Cross-Equatorial Cell (CEC) for the period 1955–1990 (Schoenefeldt and Schott 2006) and Subtropical Cell (STC) from 1992 to 2000 (Lee 2004), even a recovery of the Indian Ocean STC over 2000–2006 (Lee and McPhaden 2008) may be associated with the SST warming. Besides these local heat transports, Pacific decadal variability via atmospheric bridge and a slowing Indonesian Throughflow (ITF) transport have an important impact on multi-decadal changes in the TIO SST (Annamalai et al. 2005; Ashok et al. 2004). Specifically, ENSO has played an important role in modulating the western Indian Ocean warming since the 1950s (Roxy et al. 2014). The intensification of IOBM from the late nineteenth to the early twentieth century is modulated by multi-decadal variations in ENSO (Chowdary et al. 2012). Due to the complexity and richness of these issues, a great deal of efforts should be made to have a comprehensive understanding of the physical mechanisms for the TIO SST warming pattern.

Acknowledgments We wish to thank Shang-Ping Xie for constructive suggestions. We are grateful to the editor. We also thank two anonymous reviewers who provided constructive reviews of this study. This work was supported by the National Basic Research Program of China (2012CB955604 and 2011CB309704), the National Outstanding Youth Science Fund Project of China (41425019), the Strategic Priority Research Program of the Chinese Academy of Sciences (XDA05090402) and the National Natural Science Foundation of China (41275083 and 91337105).

References

Alory G, Meyers G (2009) Warming of the upper Equatorial Indian Ocean and changes in the heat budget (1960–99). J Clim 22:93–113

Alory G, Wijffels S, Meyers G (2007) Observed temperature trends in the Indian Ocean over 1960–1999 and associated mechanisms. Geophys Res Lett 34(2)

Annamalai H, Potemra J, Murtugudde R, McCreary J (2005) Effect of preconditioning on the extreme climate events in the Tropical Indian Ocean. J Clim 18:3450–3469

Ashok K, Guan Z, Yamagata T (2003) Influence of the Indian Ocean Dipole on the Australian winter rainfall. Geophys Res Lett 30(15)

Ashok K, Chan WL, Motoi T, Yamagata T (2004) Decadal variability of the Indian Ocean dipole. Geophys Res Lett 31(24)

Bader J, Latif M (2003) The impact of decadal-scale Indian Ocean sea surface temperature anomalies on Sahelian rainfall and the North Atlantic Oscillation. Geophys Res Lett 30(22)

Barnett TP, Pierce DW, AchutaRao KM, Gleckler PJ, Santer BD, Gregory JM, Washington WM (2005) Penetration of human-induced warming into the world's oceans. Science 309:284–287

Chowdary J, Xie S-P, Tokinaga H, Okumura YM, Kubota H, Johnson N, Zheng X-T (2012) Interdecadal variations in ENSO teleconnection to the Indo-Western Pacific for 1870–2007. J Clim 25:1722–1744

Du Y, Xie S-P (2008) Role of atmospheric adjustments in the tropical Indian Ocean warming during the 20th century in climate models. Geophys Res Lett 35:L08712

Du Y, Xie S-P, Huang G, Hu K (2009) Role of air–sea interaction in the long persistence of El Niño-Induced North Indian Ocean warming. J Clim 22:2023–2038

Du Y, Xie S-P, Yang Y-L, Zheng X-T, Liu L, Huang G (2013) Indian Ocean variability in the CMIP5 multimodel ensemble: the basin mode. J Clim 26:7240–7266

Giannini A, Saravanan R, Chang P (2003) Oceanic forcing of Sahel rainfall on interannual to interdecadal time scales. Science 302:1027–1030

Gillett N, Zwiers F, Weaver A, Hegerl G, Allen M, Stott P (2002) Detecting anthropogenic influence with a multi-model ensemble. Geophys Res Lett 29:31-31–31-34

Godfrey JS, Hu R-J, Schiller A, Fiedler R (2007) Explorations of the annual mean heat budget of the tropical Indian Ocean. Part I: studies with an idealized model. J Clim 20:3210–3228

Harrison D, Carson M (2007) Is the World Ocean warming? Upper-ocean temperature trends: 1950–2000. J Phys Oceanogr 37:174–187

Hegerl GC, Bindoff NL (2005) Warming the world's oceans Science 309:254–255

Hegerl GC, von Storch H, Hasselmann K, Santer BD, Cubasch U, Jones PD (1996) Detecting greenhouse-gas-induced climate change with an optimal fingerprint method. J Clim 9:2281–2306

Hoerling M, Kumar A (2003) The perfect ocean for drought. Science 299:691–694

Hoerling MP, Hurrell JW, Xu T, Bates GT, Phillips A (2004) Twentieth century North Atlantic climate change. Part II: understanding the effect of Indian Ocean warming. Clim Dyn 23:391–405

Hoerling M, Hurrell J, Eischeid J, Phillips A (2006) Detection and attribution of twentieth-century northern and southern African rainfall change. J Clim 19:3989–4008

Huang B, Kinter JL (2002) Interannual variability in the tropical Indian Ocean. J Geophys Res Ocean (1978–2012) 107:20-21–20-26

Karoly DJ, Wu Q (2005) Detection of regional surface temperature trends. J Clim 18:4337–4343

Knutson T, Delworth T, Dixon K, Stouffer R (1999) Model assessment of regional surface temperature trends (1949–1997). J Geophys Res 104:30981–30996

Knutson TR et al (2006) Assessment of twentieth-century regional surface temperature trends using the GFDL CM2 coupled models. J Clim 19:1624–1651

Krishnan R, Ramesh K, Samala B, Meyers G, Slingo J, Fennessy M (2006) Indian Ocean-monsoon coupled interactions and impending monsoon droughts. Geophys Res Lett 33(8)

Lau N-C, Leetmaa A, Nath MJ (2006) Attribution of Atmospheric Variations in the 1997–2003 Period to SST Anomalies in the Pacific and Indian Ocean Basins. J Clim 19:3607–3628

Lee T (2004) Decadal weakening of the shallow overturning circulation in the South Indian Ocean. Geophys Res Lett 31(18)

Lee T, McPhaden MJ (2008) Decadal phase change in large-scale sea level and winds in the Indo-Pacific region at the end of the 20th century. Geophys Res Lett 35(1)

Levitus S, Antonov JI, Boyer TP, Stephens C (2000) Warming of the world ocean. Science 287:2225–2229

Levitus S, Antonov J, Boyer T (2005) Warming of the world ocean, 1955–2003. Geophys Res Lett 32(2)

Li T, Wang B, Chang C, Zhang Y (2003) A theory for the Indian Ocean Dipole-Zonal Mode. J Atmos Sci 60:2119–2135

Li H, Dai A, Zhou T, Lu J (2010) Responses of East Asian summer monsoon to historical SST and atmospheric forcing during 1950–2000. Clim Dyn 34:501–514

Liu L, Xie S-P, Zheng X-T, Li T, Du Y, Huang G, Yu W-D (2013) Indian Ocean variability in the CMIP5 multi-model ensemble: the zonal dipole mode. Clim Dyn 43:1715–1730

Lu J, Greatbatch RJ, Peterson KA (2004) Trend in Northern Hemisphere winter atmospheric circulation during the last half of the twentieth century. J Clim 17:3745–3760

Pierce DW, Barnett TP, AchutaRao KM, Gleckler PJ, Gregory JM, Washington WM (2006) Anthropogenic warming of the oceans: observations and model results. J Clim 19:1873–1900

Rayner N et al (2003) Global analyses of sea surface temperature, sea ice, and night marine air temperature since the late nineteenth century. J Geophys Res 108(D14)

Roxy MK, Ritika K, Terray P, Masson S (2014) The curious case of Indian Ocean warming. J Clim 27:8501–8509

Santer BD et al (2007) Identification of human-induced changes in atmospheric moisture content. Proc Natl Acad Sci 104:15248–15253

Santer BD et al (1995) Ocean variability and its influence on the detectability of greenhouse warming signals. J Geophys Res Ocean (1978–2012) 100:10693–10725

Santer BD et al (2004) Identification of anthropogenic climate change using a second-generation reanalysis. J Geophys Res 109(D21)

Schneider EK, Fan M (2012) Observed decadal North Atlantic tripole SST variability. Part II: diagnosis of mechanisms. J Atmos Sci 69:51–64

Schoenefeldt R, Schott FA (2006) Decadal variability of the Indian Ocean cross-equatorial exchange in SODA. Geophys Res Lett 33(8)

Smith TM, Reynolds RW, Peterson TC, Lawrimore J (2008) Improvements to NOAA's historical merged land-ocean surface temperature analysis (1880–2006). J Clim 21:2283–2296

Stocker TF et al (2013) Climate change 2013: the physical science basis intergovernmental panel on climate change, working group I contribution to the IPCC fifth assessment report (AR5). Cambridge Univ Press, New York

Stott PA (2003) Attribution of regional-scale temperature changes to anthropogenic and natural causes. Geophys Res Lett 30(14)

Taylor KE, Stouffer RJ, Meehl GA (2009) A summary of the CMIP5 experiment design WCRP, submitted

Taylor KE, Stouffer RJ, Meehl GA (2012) An overview of CMIP5 and the experiment design. Bull Am Meteorol Soc 93:485–498

Terray P, Dominiak S (2005) Indian Ocean sea surface temperature and El Niño-Southern Oscillation: a new perspective. J Clim 18:1351–1368

Tokinaga H, Xie S-P, Deser C, Kosaka Y, Okumura YM (2012) Slowdown of the Walker circulation driven by tropical Indo-Pacific warming. Nature 491:439–443

Trenberth KE, Fasullo JT (2009) Global warming due to increasing absorbed solar radiation. Geophys Res Lett 36(7)

Vecchi GA, Soden BJ (2007) Global warming and the weakening of the tropical circulation. J Clim 20:4316–4340

Vecchi GA, Soden BJ, Wittenberg AT, Held IM, Leetmaa A, Harrison MJ (2006) Weakening of tropical Pacific atmospheric circulation due to anthropogenic forcing. Nature 441:73–76

Wu Q, Karoly DJ (2007) Implications of changes in the atmospheric circulation on the detection of regional surface air temperature trends. Geophys Res Lett 34(8)

Xie S-P, Annamalai H, Schott F, McCreary J Jr (2002) Origin and predictability of South Indian Ocean climate variability. J Clim 15:864–874

Xie S-P, Deser C, Vecchi GA, Ma J, Teng H, Wittenberg AT (2010a) Global warming pattern formation: sea surface temperature and rainfall. J Clim 23:966–986

Xie S-P, Du Y, Huang G, Zheng X-T, Tokinaga H, Hu K, Liu Q (2010b) Decadal Shift in El Niño Influences on Indo-Western Pacific and East Asian Climate in the 1970s. J Clim 23:3352–3368

Xie S-P, Lu B, Xiang B (2013) Similar spatial patterns of climate responses to aerosol and greenhouse gas changes. Nat Geosci 6:828–832

Yu L, Weller RA (2007) Objectively analyzed air-sea heat fluxes for the global ice-free oceans (1981–2005) Bull Amer Meteor Soc 88:527–539

Zheng X-T, Xie S-P, Vecchi GA, Liu Q, Hafner J (2010) Indian Ocean dipole response to global warming: analysis of ocean–atmospheric feedbacks in a coupled model. J Clim 23:1240–1253